9 August 1996

ELSEVIER

Chemical Physics Letters 258 (1996) 171–179

CHEMICAL PHYSICS LETTERS

Dissociative photodetachment dynamics of $O_2^- \cdot (H_2O)$

C.R. Sherwood, R.E. Continetti

Department of Chemistry and Biochemistry, University of California, San Diego, 9500 Gilman Drive, La Jolla, CA 92093-0314, USA

Received 4 April 1996

Abstract

The dynamics of dissociative photodetachment in $O_2^- \cdot (H_2O)$ were studied using the technique of fast-beam photofragment translational spectroscopy. The kinetic energy and angular distributions of the neutral molecules produced by dissociative photodetachment ($O_2^- \cdot (H_2O) + h\nu \rightarrow O_2 + H_2O + e^-$) were recorded at 523.6, 349.0 and 261.8 nm. Dissociative photodetachment is observed to occur at all of these wavelengths with nearly identical kinetic energy release. The product angular distributions from dissociative photodetachment are slightly anisotropic and exhibit a small wavelength dependence. These results suggest that dissociative photodetachment of $O_2^- \cdot (H_2O)$ occurs via Franck–Condon excitation to a weakly repulsive region of the $O_2 \cdot (H_2O)$ potential energy surface.

1. Introduction

Due to low bond energies and electron affinities a wide variety of processes can contribute to the photochemistry of weakly bound cluster anions. One of these processes is dissociative photodetachment (DPD), in which a free electron and two (or more) neutral fragments are produced by photon absorption. Although the photodetachment of cluster anions has been extensively studied using photoelectron spectroscopy [1–3], the dynamics of DPD has received little attention. We have recently applied photofragment translational spectroscopy to measuring the kinetic energy and angular distributions of the molecular products from DPD [4,5]. In the present work, we extend these studies to measure the dynamics of DPD in the $O_2^- \cdot (H_2O)$ cluster.

Our previous studies of the tetroxide ion, O_4^-, revealed large translational energy releases ($E_T \geq 0.4$ eV) and a strong wavelength dependence in the dynamics of DPD, ($O_4^- + h\nu \rightarrow O_2 + O_2 + e^-$) [4,5]. This observation showed that photodetachment of O_4^- leaves the nascent O_2 molecules in a very repulsive region of the neutral potential energy surface. This illustrates that the bonding interaction in O_4^-, which may involve either electron delocalization or resonant charge transfer between the two O_2 moieties [6], leads to significant rearrangement of the nuclear configuration over that expected in the $(O_2)_2$ van der Waals dimer. The bonding in the prototypical superoxide–water cluster, $O_2^- \cdot (H_2O)$, is thought to be dominated by electrostatic interactions [7]. Thus, a study of the translational energy release in the DPD of $O_2^- \cdot (H_2O)$ may reveal an alternative limit for the dynamics of DPD from that observed in the case of O_4^-. In the work reported here, it is found that $O_2^- \cdot (H_2O)$ exhibits small translational energy release and little wavelength dependence in the dynamics of DPD. In the following paragraphs, previous work on the photochemistry of $O_2^- \cdot (H_2O)$ is reviewed, followed a description of the experimental techniques and the results of this study.

PII S0009-2614(96)00610-0

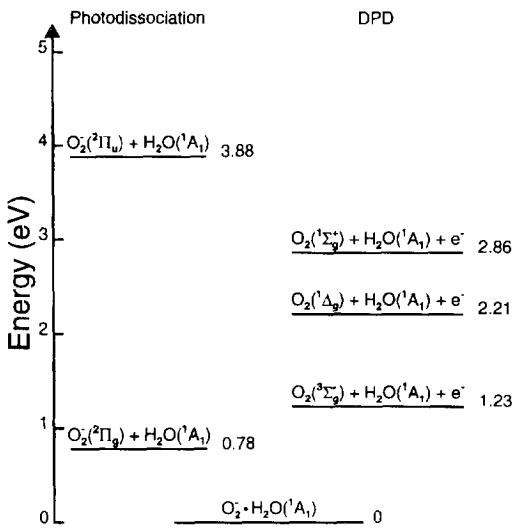

Fig. 1. Energy level diagram for $O_2^- \cdot (H_2O)$. The left column gives the minimum energy required for photodissociation of $O_2^- \cdot (H_2O)$ into the specified products. The right column gives the minimum energy required for dissociative photodetachment (DPD), assuming the production of zero kinetic energy electrons.

The photodestruction processes of $O_2^- \cdot (H_2O)$ were investigated in a series of measurements in the 1970s [8–11]. In the wavelength range from 250–850 nm, an unstructured total photodestruction cross-section was observed. This cross-section appeared to be similar to the photodetachment cross section of O_2^-, except for a shift to shorter wavelengths. The similarity in cross-sections led to the suggestion that the predominant pathway for photodestruction was dissociative photodetachment [10]:

$$O_2^- \cdot (H_2O) \rightarrow O_2 + H_2O + e^-. \quad (1)$$

This assignment seemed plausible since dissociative photodetachment was known to be energetically accessible for the wavelengths at which photodestruction was observed. The bond energy of $O_2^- \cdot (H_2O)$ relative to $O_2^- + H_2O$ had been previously measured to be 0.78 eV [12,13], and the electron affinity (0.451 eV) of O_2^- was known [14], yielding an energetic threshold for dissociative photodetachment of 1.23 eV (see Fig. 1). This threshold is ~ 0.6 eV lower in energy than the measured threshold for photodestruction (~ 1.8 eV) [9].

Collision-induced dissociation, photodetachment and photodissociation of $O_2^- \cdot (H_2O)$ have since been investigated by Johnson and co-workers [15]. The only ionic product observed in collision-induced dissociation was O_2^-. This result suggests that the extra electron is localized on the O_2 species. The photoelectron spectrum of $O_2^- \cdot (H_2O)$ at 355 nm revealed two broad overlapping features similar in shape to the envelopes correlated with photodetachment of bare O_2^- into both the $X\,^3\Sigma_g^-$ and $a\,^1\Delta_g$ vibrational manifolds of O_2. Moreover, the photoelectron angular distribution for each feature was similar to the angular distributions from the photodetachment of bare O_2^- into these electronic states. Johnson and co-workers also observed ionic photodissociation products from $O_2^- \cdot (H_2O)$, but only at wavelengths ≤ 266 nm. The photodissociation products are thought to originate from excitation of the known dissociative $A\,^2\Pi_u \leftarrow X\,^2\Pi_g$ transition of O_2^- [16]. This work was later extended to study the photodissociation of larger clusters, $O_2^- \cdot (H_2O)_n$ ($n \leq 33$) in which the analog of the O_2^- ($A\,^2\Pi_u \leftarrow X\,^2\Pi_g$) transition persists [17]. The similarity of both the photoelectron spectrum and photodissociation threshold to O_2^- experimentally suggests that bonding in the $O_2^- \cdot (H_2O)$ anion is chiefly an ion–dipole interaction, leaving O_2^- intact.

Johnson and co-workers made further observations, however, that suggest $O_2^- \cdot (H_2O)$ cannot be completely described as an ion–dipole bound species [15]. The maximum intensity in the photoelectron spectrum (i.e. vertical detachment energy) of $O_2^- \cdot (H_2O)$ is shifted by more than the dissociation energy of the ionic complex relative to the photoelectron spectrum of O_2^-. This implies that the geometries of the O_2^- and H_2O moieties in the complex are not the same as the isolated species. Additionally, some of the observed photodissociation products could only be accounted for by the activation of further intra-complex reactions involving both the O^- and O fragments from the analog of the $A \leftarrow X$ transition of O_2^- [15].

$O_2^- \cdot (H_2O)$ has been the subject of several ab initio calculations. These theoretical investigations have given results in reasonable agreement with the experimental thermochemistry [13]. The structure of the anion, however, is less well-defined. Ohta and Morokuma [18] have carried out spin-unrestricted Hartree–Fock (UHF) calculations with a 3-21G* basis set, indicating several low-lying planar C_s structures, all within ≈ 0.1 eV of each other. Curtiss

et. al [7] performed UHF (MP3/6-31G*) calculations and found both singly and doubly hydrogen-bonded minima on the $O_2^- \cdot (H_2O)$ potential energy surface. Lee and Dyke [19] extended this work with both larger basis sets and higher-level perturbation theory and found the planar doubly hydrogen-bonded C_{2v} structure to be the minimum. The energy differences between the different isomers are small, however, so the potential energy surface of $O_2^- \cdot (H_2O)$ is relatively flat near the equilibrium geometry.

2. Experimental

The experiment uses coincidence-based translational energy spectroscopy in a fast-ion beam. Mass-selected $O_2^- \cdot (H_2O)$ anions are intersected with a laser pulse and the resulting photofragments are measured by a two-particle time- and position-sensitive detector. The spectrometer can efficiently detect both molecular fragments, either neutral or ionic, from a binary dissociative event in coincidence. The measured times and positions of coincident fragments allow the direct calculation of fragment mass ratio, translational energy release, and recoil angle for each detected event [20,21]. This apparatus has been described in detail [22] and is only briefly reviewed here.

The anion source and ion-beam line are similar to that employed by Neumark and co-workers to study the photodissociation of free radicals [21]. $O_2^- \cdot (H_2O)$ is formed by crossing a pulsed supersonic expansion of O_2 and trace amounts of water vapor with a 1 keV electron beam [23]. The anions are skimmed, accelerated to 2–4 keV, and mass-selected by time-of-flight. Anions arrive at the laser interaction region in mass-selected packets $\sim$ 20–50 ns wide.

The $O_2^- \cdot (H_2O)$ anions are intersected at a right angle with a linearly polarized laser pulse from the second (523.6 nm, 2.37 eV), third (349.0 nm, 3.55 eV), or fourth (261.8 nm, 4.74 eV) harmonic of a diode-pumped Nd:YLF laser (Spectra Physics TFR). The laser pulse is 6 ns full-width-at-half-maximum with energies of 200 μJ at 523.6 nm or 20–30 μJ at either of the ultraviolet wavelengths. The pulse is focused to a $\sim$ 0.5 mm spot at the point of intersection with the $\sim$ 1.0 mm diameter ion beam. The experiment was performed at a repetition rate of 500 Hz.

Molecular photofragments from the ion–laser interaction traverse a 96 cm flight path to a 40 mm diameter microchannel-plate (MCP) detector. The detector employs a split wedge-and-strip anode to record the time and position of incidence of both photofragments from a single dissociation [21]. The face of the detector is fixed at ground potential to allow measurement of both ionic and neutral fragments. The high velocity of the parent anion kinematically constrains the photofragment trajectories to a narrow cone directed at the detector while also providing for high detection efficiency by the MCPs. A 7 mm-wide horizontal beam stop is centered on the ion-beam axis to prevent undissociated ions and neutrals from striking the front of the MCPs.

The time and position-of-arrival of the fragments are recorded individually by the two-particle anode. False coincidences are discarded with high efficiency by applying momentum conservation to calculate the apparent center-of-mass. This must be done for all possible chemically distinct product channels. Events are rejected if the apparent center-of-mass of the two fragments at the detector is located outside an ≈ 2 mm^3 volume defined by the projection of the laser/ion beam interaction volume onto the detector. For a system with asymmetric kinematics like $O_2^- \cdot (H_2O)$, this technique provides a modest mass resolution of $m/\Delta m \approx 8$. Fragment pairs may be recorded using two different acquisition modes, where either ionic *and* neutral products or *only* neutral products are detected. An electrostatic field, located after the ion-laser interaction region, can be used to deflect residual ions and ionic fragments out of the beam. By enforcing the coincidence requirement, any events which produce ionic products are removed from data sets recorded with the deflector in use. If the deflection field is off, both neutral-neutral and anion–neutral fragment pairs are detectable in coincidence. No differences were observed between the data taken in these two modes in this experiment, leading to the conclusion that the dominant photodestruction pathway for $O_2^- \cdot (H_2O)$ is dissociative photodetachment.

Due to the measurement of both time and position of arrival, the data contain a three-dimensional record of each dissociation event [20,21]. This allows correlated translational energy and recoil angle distribu-

tions to be calculated as discussed below. The dissociation events are histogrammed in translational energy and angular distributions $N(E_T)$ and $N(\theta)$, and other distributions as required. The observed translational energy and angular distributions are altered, however, due to the geometry of the apparatus. Both the beam-stop and finite size of the detector prevent certain product translational energy and recoil angles from being detected in coincidence. In the $O_2^- \cdot (H_2O)$ experiment, products at low translational energy release are not detected efficiently due to the larger solid angle subtended by the beam-stop in the center-of-mass frame at low energies. Since the goal of the experiment is to determine the true center-of-mass translational energy and angular distributions, the experimental results must be adjusted to account for the limited detector acceptance.

3. Data analysis

The data is numerically corrected for the finite detector acceptance using a straightforward numerical procedure [21,22]. This involves calculating the fraction of events which can be detected in coincidence as a function of center-of-mass (c.m.) translational energy, E_T and polar c.m. scattering angle, θ, given the finite laboratory angular acceptance of the detector. The raw data is then divided by this detector acceptance function, to yield the acceptance corrected c.m. translational energy and angular distribution $P(E_T,\theta)$. The $P(E_T,\theta)$ is then interpreted using a least-squares fit to the standard electric dipole model [24–26]. The model describes the c.m. translational energy and angular distributions in a separable approximation as

$$P(E_T,\theta) = P(E_T)\left[1 + \beta(E_T) P_2(\cos\theta)\right]. \quad (2)$$

Here, $P_2(\cos\theta)$ is the second Legendre polynomial in $\cos\theta$, and θ is the angle between the fragment recoil direction and the electric vector of the laser. $\beta(E_T)$ is the energy-dependent anisotropy parameter describing the angular distribution and $P(E_T)$ is the center-of-mass translational energy distribution. $\beta(E_T)$ in this formula can range between the 'parallel' ($\beta = 2$, or $\cos^2\theta$) and 'perpendicular' ($\beta = -1$, or $\sin^2\theta$) limits [24].

The quality of the extracted $P(E_T)$ and $\beta(E_T)$ can be examined using forward convolution techniques to simulate the experimental results. Two forward convolution methods are used, a Monte Carlo and a grid-based method. Using the Monte Carlo method [22,27], simulated data is generated by averaging $P(E_T)$ and $\beta(E_T)$ over all of the important apparatus parameters: ion beam size, velocity and divergence; laser beam spot-size; detector geometry; and time and position resolution of the detector. These experimental distributions are importance-sampled and the simulated data is recorded event-by-event. The simulated data is then processed and histogrammed by the same code used to analyze the experimental data. In the grid-based technique, the detector acceptance function $D(E_T,\theta,\phi)$ is calculated, where ϕ is the azimuthal angle about the laser electric vector. This function provides the fraction of events that are detectable for a given center-of-mass translational energy release and recoil direction based on the apparatus geometry, ion beam velocity, and fragment mass ratio. The detector acceptance function is then multiplied by $P(E_T,\theta)$ to obtain the simulated data function $S(E_T,\theta,\phi)$:

$$S(E_T,\theta,\phi) = D(E_T,\theta,\phi) \cdot P(E_T)\left[1 + \beta(E_T) P_2(\cos\theta)\right], \quad (3)$$

which contains the acceptance-weighted intensity for all energy and angle space. Each bin in $S(E_T,\theta,\phi)$ is characterized by a center-of-mass fragment recoil velocity vector of specific length and direction relative to the electric vector of the laser. The known polarization angle of the laser in the laboratory coordinate frame provides a connection between these vectors and the ion-beam velocity vector. This relation is used to calculate the simulated detector positions, fragment radial separation, times-of-flight, etc., for each bin in $S(E_T,\theta,\phi)$. Histograms of each simulated distribution are constructed by adding the weight of each contributing bin in $S(E_T,\theta,\phi)$. The advantage of the grid-based method is that high-signal-to-noise simulations are obtained rapidly. The Monte Carlo method has the advantage of providing a more accurate simulation of the experiment by including additional sources of experimental broadening.

4. Results

Raw translational energy release spectra are presented in Fig. 2 from the photodestruction of $O_2^- \cdot (H_2O)$ at 523.6, 349.0, and 261.8 nm. The spectra in this figure consist of approximately 15,000–20,000 coincident neutral–neutral pairs taken at a beam energy of 2.5 keV with the laser polarized along the ion beam direction. At each wavelength, dissociative photodetachment (Eqn. 1) was observed. No evidence was seen for ionic products, although ion photodissociation has been observed by Johnson and co-workers at wavelengths shorter than 266 nm [15]. Since the quantum yield for photodissociation of bare O_2^- is only 3% of that for photodetachment in this wavelength region [28], the ion photodissociation signal is apparently obscured by the dominant dissociative photodetachment process in our measurement.

The data for the three wavelengths are nearly identical and are characterized by a very low translational energy release (peak $E_T \sim 0.14$ eV). The similarity among the spectra implies that the translational energy release is independent of the final electronic and vibrational state of the products. Photoelectron spectra of $O_2^- \cdot (H_2O)$ taken by Johnson and co-workers [15] at 355 nm reveal that excitation is occurring to the vibrational manifolds of both O_2 ($X\,^3\Sigma_g^-$) and ($a\,^1\Delta_g$). Due to the blue-shifted electron binding energy in $O_2^- \cdot (H_2O)$, only $X\,^3\Sigma_g^-$ should be produced at 523.6 nm, while $X\,^3\Sigma_g^-$, $a\,^1\Delta_g$, and $b\,^1\Sigma_g^+$ are accessible at 261.8 nm.

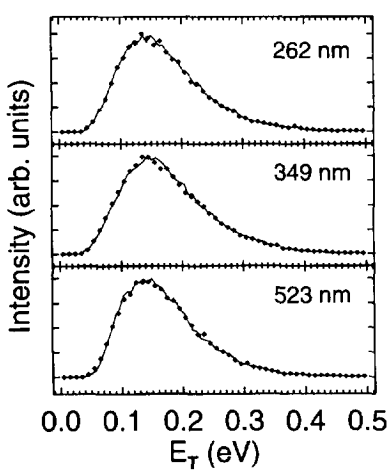

Fig. 2. Raw translational energy release spectra ($N(E_T)$) and Monte Carlo simulations of the dissociative photodetachment of $O_2^- \cdot (H_2O)$. The simulations (solid lines) and experimental data (points) are presented for 523.6, 349.0 and 261.8 nm as labelled.

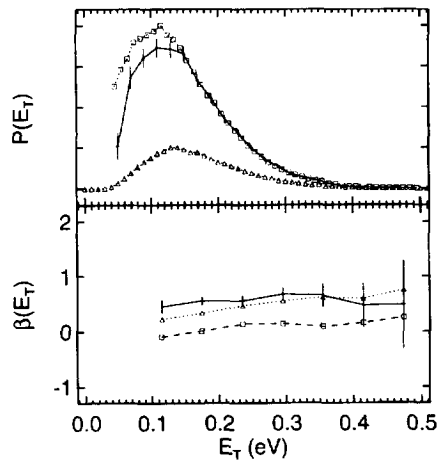

Fig. 3. $P(E_T)$ and $\beta(E_T)$ distributions for $O_2^- \cdot (H_2O)$. In the top frame, the forward convolution $P(E_T)$ is shown as squares with a dashed line, the detector-acceptance-corrected $P(E_T)$ is shown as a solid line with $\pm 2\sigma$ error bars, and the raw translational energy release spectrum is shown as triangles. These correspond to the results at 349.0 nm, and they are plotted on a common scale to illustrate the effects of the detector acceptance. In the bottom frame, $\beta(E_T)$ for all three wavelengths are plotted. Data at 523.6 nm (solid line), 349.0 nm (dotted line), and 261.8 nm (dashed line) show that the angular distribution changes with wavelength. For reasons of clarity, only the error bars ($\pm 2\sigma$) for 523.6 nm are shown in the lower frame.

After correcting for detector acceptance, the data at each wavelength is least-squares-fit to extract $P(E_T)$ and $\beta(E_T)$. The extracted $P(E_T)$ and $\beta(E_T)$ are usually reported without alteration; this procedure was followed for the O_4^- data previously presented [4,5]. Unfortunately, the fitting algorithm has difficulty with the low translational energy range due to the limited angular acceptance imposed by the detector beam-stop. In these experiments, *no* events with $E_T < 0.040$ eV were detectable. Unlike O_4^-, a large portion of the data for $O_2^- \cdot (H_2O)$ falls in this energy range $E_T < 0.15$ eV. The shortcoming of the fit was evident in forward-convolution simulations of the experiment performed using the fit $P(E_T)$ and $\beta(E_T)$ as inputs.

The fitting problem can be overcome by using the forward convolution approach to improve the $P(E_T)$

and $\beta(E_T)$ by direct comparison to the experimental results. Since a three-dimensional record of each dissociation event is available, the data inherently provide other experimental distributions for comparison, such as time-of-flight, laboratory angles, and radial separation of the fragments. The grid-based technique is used to simulate these other distributions as well as the laboratory translational energy and angular distribution, while $\beta(E_T)$ and $P(E_T)$ are adjusted to obtain an improved fit. The grid-based technique was chosen due to the reduced fitting time. Once a good fit was achieved, a single Monte Carlo simulation is run for verification.

The $P(E_T)$ distributions for the three wavelengths are indistinguishable within experimental error, as expected from the similarity of the raw translational energy spectra. The forward-convolution $P(E_T)$, the raw detector-acceptance-corrected $P(E_T)$, and the raw translational energy release spectrum recorded at 349.0 nm are shown on a common scale in the top frame of Fig. 3. The difference between the $P(E_T)$'s and the raw data illustrates the large effect of the detector acceptance on the relative intensity of the measured spectrum at low translational energy releases. The difference between the adjusted and unaltered $\beta(E_T)$ and $P(E_T)$ is an increase in the forward-convolution-fit $P(E_T)$ at energies $E_T < 0.15$ eV, as shown in Fig. 3. The $P(E_T)$ peak (0.11 eV) shifts down from the observed peak $E_T \approx 0.14$ eV in the raw data.

In contrast to $P(E_T)$, the $\beta(E_T)$ distributions for the three wavelengths show a greater variation. $\beta(E_T)$ is shown for 523.6, 349.0 and 261.8 nm in the lower frame of Fig. 3. At 523.6 nm, the angular distribution is characterized by $\beta \sim 0.5$ throughout the observed energy range. β is less parallel (~ 0.3) at 349.0 nm and the data at 261.8 nm is nearly isotropic ($\beta \sim 0.0$). The $\beta(E_T)$ reveal no statistically significant variation as a function of translational energy release.

The quality of the final forward convolution $P(E_T)$ and $\beta(E_T)$ distributions is illustrated in Figs. 2 and 4. In these figures, Monte Carlo simulations of the raw translational energy release spectra and center-of-mass angular distributions are shown, respectively. In these simulations the $P(E_T)$ and $\beta(E_T)$ distributions are used as inputs to the Monte Carlo simulation. Good agreement with the data is observed. The change in the angular distribution of the fragments as a function of wavelength can also be seen in Fig. 4. The angular distribution for the 523.6 nm data ($\beta \approx 0.5$) is somewhat broader than the 261.8 nm data ($\beta \approx 0.0$), as expected in this case with the electric vector of the laser beam linearly polarized along the ion beam direction.

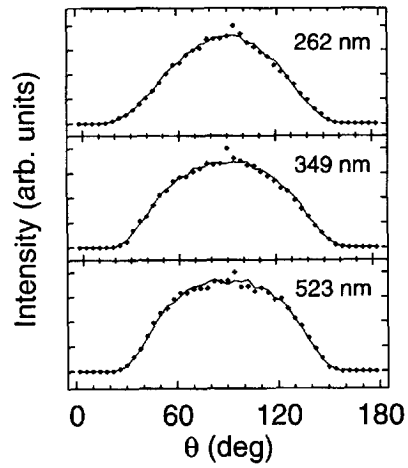

Fig. 4. Monte Carlo simulations of the fragment angular distribution $N(\theta)$ relative to the electric vector of the laser at 523.6, 349.0 and 261.8 nm as labelled. Simulations are shown as solid lines and the raw angular distributions as points.

5. Discussion

The $P(E_T)$ distributions measured from the dissociative photodetachment of $O_2^- \cdot (H_2O)$ indicate that product internal and translational energies are nearly independent. The translational energy release spectra obtained at photon energies from 2.37 to 4.74 eV show no statistical difference, while photoelectron spectra taken by Johnson [15] indicate that both vibrational and electronic excitation of the O_2 moiety occurs upon photodetachment. These observations lead to two conclusions: (1) the translational energy release for a specific set of product states is unaffected by the amount of energy carried away by the photoelectron; and (2) the dissociation pathways leading to different product states are characterized by the same translational energy release. The first conclusion simply states that the dynamics in $O_2^- \cdot (H_2O)$ appear to be completely describable under

the Franck–Condon principle, i.e. that the electron departure and nuclear readjustment on the neutral surface are effectively uncoupled events. The evidence for this conclusion is the lack of wavelength dependence in $P(E_T)$. The second conclusion is less intuitive and perhaps more surprising. As shown by the wide range of photoelectron energies measured by Johnson [15], different electronic states of the neutral complex must be accessed in photodetachment. Differences in the shape of these potential energy surfaces would be expected to yield variations in the translational energy release. Evidently the topology of these surfaces are similar and are not affecting the $O_2^- \cdot (H_2O)$ $P(E_T)$. An additional conclusion that can be drawn is that transfer of internal energy in O_2 and H_2O to the reaction coordinate is highly inefficient in the neutral $O_2 \cdot (H_2O)$ complex.

The most plausible explanation of the observed results is that photodetachment is leaving the neutral complex in a repulsive region of the potential where the internal structure of the O_2 and H_2O species has little influence on the dissociation dynamics. Theoretical calculations of the $O_2^- \cdot (H_2O)$ structure put the oxygen atom of the water molecule at ~ 2.8 Å from the center of the O_2^- species [19]. Reed, et al. [29] have studied the neutral $O_2 \cdot (H_2O)$ complex at the Hartree–Fock (MP2/6-31G*) level, and found a singly hydrogen-bonded C_s structure with the oxygen atom of water at ~ 3.8 Å from the center of O_2. This complex was found to have a binding energy of only 0.04 eV. Vertical photodetachment thus places the molecules ~ 1 Å closer together than the equilibrium geometry on the neutral surface. It is not surprising then that there is repulsion between the O_2 and H_2O molecules, causing the complex to dissociate. The data indicate, however, that there is little dependence of this repulsive potential on the electronic and vibrational states of O_2 and H_2O.

A second possibility is that an $O_2 \cdot (H_2O)$ complex is formed by photodetachment, with subsequent unimolecular decomposition. In a complex with only five atoms, and a considerable change in internal energy as the photon energy is increased from 2.37 to 4.74 eV, it would appear likely that some of this energy would be transferred to the reaction coordinate. Given that there is no change in the translational energy release and the large equilibrium geometry change between $O_2 \cdot (H_2O)$ and $O_2^- \cdot (H_2O)$ it appears unlikely that a bound region on the $O_2 \cdot (H_2O)$ potential energy surface is reached.

The angular distribution of the O_2 and H_2O fragments does change, however, as the photon energy increases. The presence of anisotropy in the angular distributions implies that there is some degree of alignment of the neutrals produced by photodetachment. Any alignment produced in dissociative photodetachment is determined by the symmetry of the initial (anion) and final (electron + neutral complex) states [30,31]. The alignment change as a function of wavelength may arise from variations in the population of excited electron + neutral states with different symmetry or from an electron-energy-dependent photoelectron continuum for the individual electron + neutral states. At higher photon energies, new excited neutral potential energy surfaces may become populated and would be expected to lead, for example, to the production of O_2 $a^1\Delta_g$ and $b^1\Sigma_g^+$ fragment states. Photofragment angular distributions involving production of these excited states may each be characterized by a specific β due to the different symmetry and photoelectron continuum associated with these states [31]. The alignment observed in the unresolved spectra, measured as the anisotropy of the photofragment angular distribution, could thus be expected to change as the relative populations of the states change. Similarly, if the nature of the photoelectron continuum for individual states of the neutral complex is a function of electron energy, the alignment would be expected to change as a function of wavelength [31,32]. A detailed interpretation of the anisotropy parameters is not possible at this time, as they depend not only on the above considerations, but also on the orientation of the transition dipole relative to the recoil axis [26]. This orientation is presently unknown and may be only weakly fixed in the $O_2^- \cdot (H_2O)$ complex.

The dynamics of DPD in $O_2^- \cdot (H_2O)$ are very different than the wavelength-dependent dynamics previously found for the DPD of O_4^- [5]. In O_4^-, the translational energy release changes as a function of product internal states. In addition, for some O_4^- transitions, interactions between the departing photoelectron and the neutral core influence the partitioning of available energy in an inherently non-Franck–Condon process [33]. No evidence for phenomena of this type are seen in the $P(E_T)$ distribu-

tions of $O_2^- \cdot (H_2O)$. The observation of alignment in the photofragments is in accord, although considerably smaller in magnitude, with the previous measurements on the dissociative photodetachment of O_4^-. An important difference between $O_2^- \cdot (H_2O)$ and O_4^-, however, is that the range of the exit-channel interaction between the departing electron and photodetached neutral is much larger in the former due to the permanent dipole of H_2O [34].

6. Conclusions

Fragment energy and angular distributions from the photodestruction of $O_2^- \cdot (H_2O)$ at 523.6, 349.0 and 261.8 nm have been obtained using photofragment translational spectroscopy in a fast ion beam. The data indicate that the predominant photodestruction pathway is dissociative photodetachment at these wavelengths. The c.m. translational energy release distribution, $P(E_T)$ are independent of photon energy and peak at low $E_T \sim 0.10$ eV. In conjunction with previous photoelectron spectra of $O_2^- \cdot (H_2O)$ [15], the data indicate that the electronic and vibrational state of the neutral fragments have little influence on the dissociation coordinate. These results are consistent with dissociation on a weakly repulsive neutral surface. The angular distribution of the photofragments reveal that alignment of the neutral complex is produced in photodetachment. The angular distribution changes as a function of excitation energy, showing the influence of either multiple dissociative states of the neutral complex with different symmetry or an electron-energy dependent photoelectron continuum.

The results from this study and our recent work on O_4^- reveal that a wide range of dynamics is possible in systems undergoing dissociative photodetachment. In both of these systems, dissociative photodetachment is the dominant photodestruction pathway and it is anticipated that this process will be an important photodestruction channel in other cluster anions as well. As seen in O_4^-, however, photodissociation may also play a significant role in the photodestruction of cluster anions. Future experiments making use of photoelectron-neutral–neutral coincidence spectroscopy, in which the kinetic energy of the electron is measured in coincidence with the photofragment translational energy release [33], will be useful in further clarifying the photodestruction dynamics of $O_2^- \cdot (H_2O)$ and other cluster anions.

Acknowledgements

This work was supported by the Chemistry Division of the National Science Foundation. REC acknowledges support from a Camille and Henry Dreyfus New Faculty Award and a 1994 Packard Fellowship in Science and Engineering.

References

[1] K.M. Ervin and W.C. Lineberger, in: Advances in gas phase ion chemistry, Vol. 1; ed. N.G. Adams and L.M. Babcock, (JAI Press, Greenwich, CT, 1992).
[2] D.M. Neumark, Accts. Chem. Res. 26 (1993) 33.
[3] S.T. Arnold, J.G. Eaton, D. Patel-Misra, H.W. Sarkas and K.H. Bowen, in: Ion and cluster ion spectroscopy and structure, ed. J.P. Maier (Elsevier, New York, 1989) pp. 417–472.
[4] C.R. Sherwood, M.C. Garner, K.A. Hanold, K.M. Strong and R.E. Continetti, J. Chem. Phys. 102 (1995) 6949.
[5] R.E. Continetti, C.R. Sherwood, M.C. Garner, K.A. Hanold and K.M. Strong, SPIE Conference on laser techniques for state-Selected and state-to-state chemistry III, Vol. 2548, (1995) 122.
[6] M.J. DeLuca, C.C. Han and M.A. Johnson, J. Chem. Phys. 93 (1990) 268.
[7] L.A. Curtiss, C.A. Melendres, A.E. Reed, and F. Weinhold, J. Comp. Chem. 7 (1986) 294.
[8] P.C. Cosby, J.H. Ling, J.R. Peterson, and J.T. Moseley, J. Chem. Phys. 65 (1976) 5267.
[9] G.P. Smith, L.C. Lee, P.C. Cosby, J.R. Peterson, and J.T. Moseley, J. Chem. Phys. 68 (1978) 3818.
[10] L.C. Lee and G.P. Smith, J. Chem. Phys. 70 (1979) 1727.
[11] R.V. Hodges, L.C. Lee, and J.T. Moseley, J. Chem. Phys. 72 (1980) 2998.
[12] M. Arshadi and P. Kebarle, J. Phys. Chem. 74 (1970) 1483.
[13] R. Yamdagni, J.D. Payzant, and P. Kebarle, Can. J. Chem. 51 (1973) 2507.
[14] M.J. Travers, D.C. Cowles and G. Barney Ellison, Chem. Phys. Lett. 164 (1989) 449.
[15] M.A. Buntine, D.J. Lavrich, C.E. Dessent, M.G. Scarton and M.A. Johnson, Chem. Phys. Lett. 216 (1993) 471.
[16] D.J. Lavrich, M.A. Buntine, D. Serxner and M.A. Johnson, J. Chem. Phys. 99 (1993) 5910.
[17] D.J. Lavrich, M.A. Buntine, D. Serxner and M.A. Johnson, J. Phys. Chem. 99 (1995) 8453.
[18] K. Ohta and K. Morokuma, J. Phys. Chem. 91 (1987) 401.
[19] E.P.F. Lee and J.M. Dyke, Mol. Phys. 74 (1991) 333.
[20] D.P. DeBruijn and J. Los, Rev. Sci. Instrum. 53 (1982) 1020.

[21] R.E. Continetti, D.R. Cyr, D.L. Osborn, D.J. Leahy and D.M. Neumark, J. Chem. Phys. 99 (1993) 2616.
[22] C.R. Sherwood, Ph.D. Thesis, University of California, San Diego (1995).
[23] M.A. Johnson, M.L. Alexander and W.C. Lineberger, Chem. Phys. Lett. 112 (1984) 285.
[24] R.N. Zare, Mol. Photochem. 4 (1972) 1.
[25] R. Bersohn and S.H. Lin, Adv. Chem. Phys. 16 (1969) 67.
[26] S.-C. Yang and R. Bersohn, J. Chem. Phys. 61 (1974) 4400.
[27] D.R. Cyr, R.E. Continetti, R.B. Metz, D.L. Osborn and D.M. Neumark, J. Chem. Phys. 97 (1992) 4937.
[28] D.J. Lavrich, M.A. Buntine, D. Serxner and M.A. Johnson, J. Chem. Phys. 99 (1993) 5910.
[29] A.E. Reed, F. Weinhold, L.A. Curtiss and D.J. Pochatko, J. Chem. Phys. 84 (1986) 5687.
[30] C.H. Greene and R.N. Zare, Ann. Rev. Phys. Chem. 33 (1982) 119.
[31] J.L. Dehmer and D. Dill, Phys. Rev. A 18 (1978) 164.
[32] J. Cooper and R.N. Zare, J. Chem. Phys. 48 (1968) 942.
[33] K.A. Hanold, C.R. Sherwood and R.E. Continetti, J. Chem. Phys. 103 (1995) 9876.
[34] N. Lane, in: Electron-molecule scattering, ed. S.C. Brown (John Wiley, New York 1979) pp. 176–181.